Computers in Industry 148 (2023) 103882

Contents lists available at ScienceDirect

Computers in Industry

journal homepage: www.sciencedirect.com/journal/computers-in-industry

Real-time layer height estimation during multi-layer directed energy deposition using domain adaptive neural networks

Liu Yang [a,b], Hoon Sohn [a,c,*], Zhanxiong Ma [a], Ikgeun Jeon [a], Peipei Liu [a,c], Jack C.P. Cheng [b]

[a] Department of Civil and Environmental Engineering, Korea Advanced Institute of Science and Technology (KAIST), Daejeon 34141, Republic of Korea
[b] Department of Civil and Environmental Engineering, The Hong Kong University of Science and Technology, Clear Water Bay, Kowloon, Hong Kong Special Administrative Region
[c] Center for 3D Printing Nondestructive Testing, Korea Advanced Institute of Science and Technology (KAIST), Daejeon 34141, Republic of Korea

ARTICLE INFO

Keywords:
Directed energy deposition
Corner layer height estimation
Domain adaptive neural networks
Knowledge transfer
Laser line scanning
Vision camera

ABSTRACT

Metal additive manufacturing (AM), such as laser direct energy deposition (DED), is gaining popularity because of its capability in manufacturing near-net-shaped complex components for various industrial applications. However, the geometry control during the DED process, especially at corners with sharp turns, remains a daunting task. To achieve geometry control, geometry estimation to identify the relationship between the process parameters and geometry attributes is vital. In this study, a real-time layer height estimation technique is developed for DED using a laser line scanner, vision camera, and domain adaptive neural networks (DaNN). An emphasis is placed on layer height estimation at sharp corners during multi-layer deposition. First, multi-layer straight-line deposition data is collected using laser line scanner and an initial layer height estimation model is constructed. Then, to efficiently achieve layer height estimation during corner deposition, an DaNN model is established using the multi-layer straight-line deposition data and the constructed initial model. The actual traverse speed at the corners is measured using a vision camera and fed into the DaNN model as one of input features. Finally, the DaNN model is updated online to further improve estimation accuracy during corner deposition. The proposed technique has been validated by DED experiments and the results show that the layer height can be estimated in 0.018 s with an average accuracy of 25.7 μm when multiple layers with an average height of 250 μm are deposited at corners with different angles.

1. Introduction

Advantages in metal additive manufacturing (AM) technologies have contributed to its rapid development in the last decades. However, geometry control of in Metal AM is still one of the main challenges to achieve zero-defect manufacturing (Caiazzo et al., 2022). According to the American Society for Testing and Materials (ASTM) standard (ASTM Committee, 2012), metal AM technologies can be classified as either powder bed fusion (PBF) or directed energy deposition (DED). PBF enables more precise control of the geometry of a printed component than DED, but the size of printable components is limited. On the other hand, DED is more attractive for manufacturing large-scale components, but its geometry is more difficult to control.

For example, the as-built layer height is often different from the as-designed layer height even when constant printing parameters are used (Tyralla et al., 2020; Xiong and Zhang, 2014; Vandone et al., 2018; Chabot et al., 2019; Liu et al., 2021). This discrepancy results from the fact that the layer height depends on uncontrollable process parameters, such as interlayer temperatures, and surface roughness of the layers, as well as other controllable process parameters. Moreover, when the layer height varies from the as-designed value, the nozzle to the top surface distance (NTSD) also deviates from the specified value and this deviation exacerbates the layer height discrepancy (Xiong and Zhang, 2014). Such layer height discrepancy often occurs at discontinuities, such as corner points, because of the sudden traverse speed change at these points (Woo et al., 2019; Thakkar and Sahasrabudhe, 2020; Pereira et al., 2021).

For geometry control of deposited layers during a DED process, it is important to identify the relationship between process parameters and geometry attributes. The process parameters include (1) controllable

* Corresponding author at: Department of Civil and Environmental Engineering, Korea Advanced Institute of Science and Technology (KAIST), Daejeon 34141, Republic of Korea.
E-mail address: hoonsohn@kaist.ac.kr (H. Sohn).

https://doi.org/10.1016/j.compind.2023.103882
Received 14 November 2022; Received in revised form 19 February 2023; Accepted 22 February 2023
Available online 6 March 2023

parameters, often called printing parameters, such as traverse speed and laser power and (2) uncontrollable parameters such as interlayer temperatures and the previous layer height. The relationship between the process parameters and the geometrical attributes has been studied based on physics-based or data-driven modeling. Physics-based models were developed to better understand the relationship between the process parameters and the geometric attributes, considering the powder material transportation (Sun et al., 2020), powder catchment (Alya and Singh, 2021), energy transfer (Wang et al., 2016), laser-material interaction (Bayat et al., 2021), and thermomechanical effect (Walker et al., 2020). However, the geometry estimation accuracy based on physics-based modeling is not sufficiently good. For example, Wirth and Wegener (2018) used physics-based finite element simulation for DED in order to predict track geometry of single-layer deposition. The maximum estimation error of the track geometry was 14% and the average estimation errors of the layer width and height were below 5.1%. Ertay et al. (2020) proposed a physics-based model considering complex local laser-material interaction and the global thermal history to predict the track geometry for deposition with 2D/3D toolpaths. The maximum layer height estimation error from this physics-based model was about 17% for single-layer multi-track deposition. Furthermore, geometry estimation based on physics-based modeling requires numerical simulation, which is often time consuming and not suitable for real-time geometry control.

To tackle these issues, alternative data-driven modeling has been pursued. Davim et al. (2008) estimated the width, height, and depth of a single track by constructing a multivariate regression model using the laser power, traverse speed, and powder feed rate as inputs. Liu et al. (2018) adopted a nonlinear analytical function to estimate the relationship between the layer width and height and the laser power, traverse speed, and powder thickness for single-layer deposition. Wang et al. (2020) constructed both physics-based and Gaussian process regression (GPR) models to predict the layer width and height, and much better prediction accuracy was achieved using the GPR model. Most data-driven modeling studies considered three principal printing parameters: the laser power, traverse speed, and powder feed rate for geometry estimation of single-layer deposition. In addition, although geometry control often becomes an issue at corners (Kono et al., 2018), the majority of the previous studies focused on the geometry estimation of straight-line deposition rather than corner deposition.

In our study, the layer height (LH) is estimated instantaneously during multi-layer corner deposition using a domain adaptive neural network (DaNN). First, an initial layer height estimation model is constructed using laser power (P), traverse speed (V), powder feed rate (Fr), layer number (N), previous layer height (preLH), previous deposition height (preDH) and nozzle to top surface distance (NTSD) as input features and trained using data from multi-layer straight-line deposition. The LH, preLH, preDH, and NTSD are obtained from a laser line scanner. Then, to achieve layer height estimation during corner deposition which includes both the straight-line part and the corner part, a DaNN model is proposed based on the constructed ANN model, in which the actual traverse speed at the corners is measured using a vision camera and fed as an input feature for the DaNN model establishment. Finally, an online updating strategy of the DaNN model is proposed to further improve estimation accuracy during corner deposition and validated for real-time layer height estimation. This study has four major contributions: (1) a layer height estimation model is developed by considering not only three principal printing parameters (P, V, Fr) but also additional process parameters (N, preLH, preDH, NTSD); (2) a DaNN model is developed to achieve layer height estimation during corner deposition; (3) online DaNN model updating is achieved to further improve the layer height estimation accuracy during corner deposition; and (4) real-time layer height estimation for corners with different angles is validated.

The remainder of this paper is organized as follows. Section 2 presents the proposed real-time layer height estimation technique, which comprises the construction of the layer height estimation model using multi-layer straight-line data, development of layer height estimation model for multi-layer corner deposition and real-time layer height estimation for multi-layer corner deposition. Section 3 describes the experimental setup. The experimental results and conclusions are provided in Sections 4 and 5, respectively.

2. Methodology

2.1. Overview of proposed technique for real-time layer height estimation

In current practice, the relationship between the process parameters and the layer height during DED is mostly estimated based on trial-and-error experiments. This study establishes the relationship from straight-line deposition experiments and uses the established relationship to help estimate the layer height during corner deposition. The proposed technique consists of three steps, as shown in Fig. 1. In the first step, multi-layer straight-line data are collected by a laser line scanner, followed by geometry extraction and feature generation. Then, the initial layer height estimation model, i.e., an ANN model, is constructed and selected among multiple candidate models based on multi-layer straight-line deposition data. To make sufficient use of multi-layer straight-line data and save effort in training another model for layer height estimation at the corners, a DaNN model is established based on the selected ANN model for multi-layer corner deposition by considering both straight-line and corner features obtained from corner deposition. One of the corner features, the traverse speed, is revised using real-time measurement from a vision camera since the traverse speed deviates from as-designed traverse speed at the corners. Finally, the DaNN model is updated online and used to estimate the layer height in real time during multi-layer corner deposition.

The selection of an initial layer height estimation model and establishment of the DaNN model is conducted offline. Then, the trained DaNN model is continuously updated during printing and used for real-time layer height estimation. Further details are described in the following sections.

2.2. Selection of initial layer height estimation model

Since there are a lot of promising machine learning algorithms, a suitable algorithm should be selected by comparison to ensure the performance (Li et al., 2021; Wang et al., 2022). In this study, the performances of multiple machine learning algorithms are compared with different combinations of input features. Also, the hyperparameters for each model have been fine-tuned using Bayesian optimization method (Snoek et al., 2012). The best model, which is an ANN model, is selected as the initial layer height estimation model, as described in the following sections.

2.2.1. Data collection and geometry extraction

The layer height is collected using laser line scanner during multi-layer straight-line deposition and it represents the average deposition height differences between neighboring layers, noted also as inter-layer height in Fig. 2. The layer height variation during DED process can be categorized as inner-layer height variation and inter-layer height variation as illustrated in Fig. 2. The inner-layer height variation is the height variation inside each layer, while the inter-layer height variation is the layer height variation among different layers. Since the inner-height variation using the state-of-art DED manufacturing technique will not cumulate and is much smaller than inter-layer height variation though preliminary experiments, the focus of this study lies on the inter-layer height variation during multi-layer straight-line deposition. Therefore, this step uses inter-layer height for the construction of initial layer height estimation model.

To scan the cross-section profiles of the deposited layer during the DED process, a laser line scanner was attached to the DED printer nozzle and moved along with the nozzle during deposition (Binega et al., 2022).

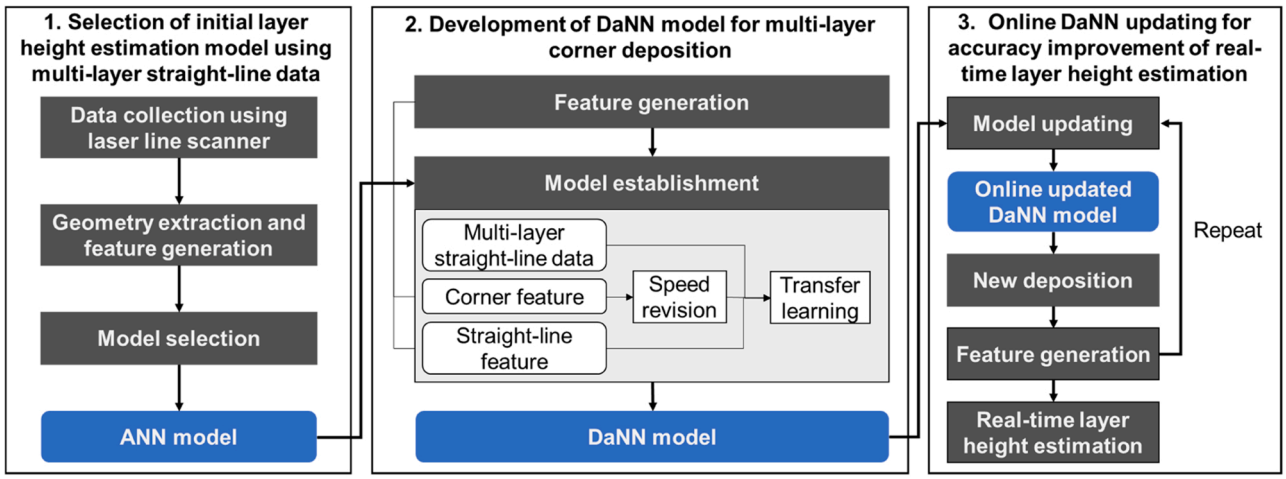

Fig. 1. Overview of the proposed technique.

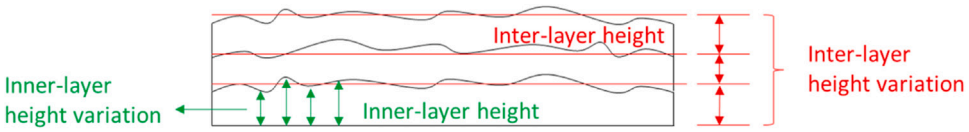

Fig. 2. Explanation of layer height.

The laser line scanner was positioned so that the projected line beam can scan the cross-sectional profiles of the deposited object. In each layer, several cross-sectional profiles are obtained and averaged to form an averaged cross-sectional profile. A spline curve is fitted for the averaged cross-sectional profile obtained from this layer, noted as a layer profile, as shown in Fig. 3. The maximum value of the fitted spline curve is defined as the deposition height at each layer. The layer height represents the increment in the deposition height when a new layer is deposited on top of the previous layer. For multi-layer straight-line deposition, the difference of deposition height and previous deposition height is defined as the layer height.

2.2.2. Feature generation

The laser power, traverse speed, feed rate, layer number, NTSD, the deposition height and layer height in the previous layer are selected as the input features of the prediction model. The layer height in the current layer is defined as the output. The laser power and traverse speed control the energy density, while the feed rate and traverse speed determine how fast the powder is deposited on the layer surface. These three features are known to be the most critical parameters that control the track geometry (Pinkerton and Li, 2004; Lee and Farson, 2016). The NTSD also influences the energy density because the NTSD affects the focusing of the laser beam, thus it is calculated and selected as an input feature. It has been reported that the layer height varies during multi-layer deposition because of inevitable disturbances, such as heat accumulation, heat conduction, interlayer temperatures, and surface condition changes as more layers are deposited (Xiong and Zhang, 2014). Therefore, the deposition height and the layer height of the previous layer and the layer number, are also added as input features since they may reflect these inevitable disturbances.

The three principal printing parameters (laser power, traverse speed, powder feed rate) are used as the default input features together with up to four additional process parameters (layer number, previous layer height, previous deposition height and nozzle to top surface distance) to be determined; thus, there are a total of 15 feature combinations considering all possible cases, as shown in Table 1. A parametric study is performed in the next step to select the best input feature combination.

2.2.3. Model selection

Six prediction models were trained and compared, namely, (1) linear regression, (2) ANN, (3) random forest, (4) AdaBoost, (5) XGboost and (6) lightGBM. The following linear regression is the simplest and most

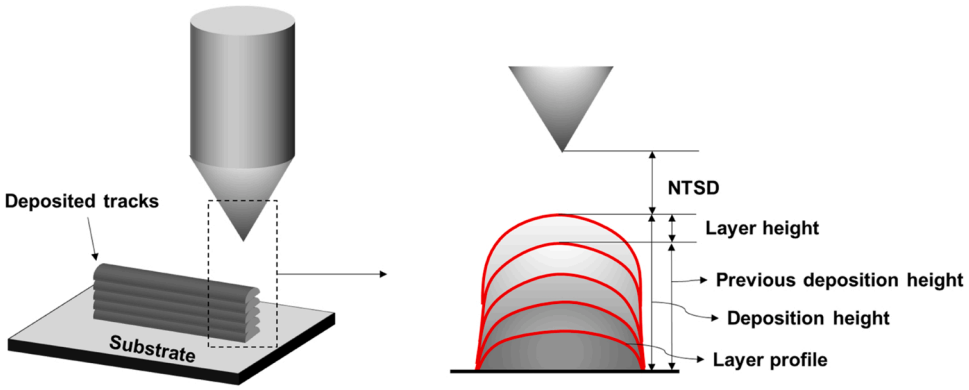

Fig. 3. Geometry extraction of multi-layer straight-line deposition.

Table 1
Feature combinations.

Index	Feature combination	Index	Feature combination
1	P, V, Fr	9	P, V, Fr, preLH, N
2	P, V, Fr, NTSD	10	P, V, Fr, preLH, preDH
3	P, V, Fr, N	11	P, V, Fr, N, preDH
4	P, V, Fr, preLH	12	P, V, Fr, NTSD, preLH, N
5	P, V, Fr, preDH	13	P, V, Fr, NTSD, preLH, preDH
6	P, V, Fr, NTSD, preLH	14	P, V, Fr, preLH, N, preDH
7	P, V, Fr, NTSD, N	15	P, V, Fr, preLH, N, preDH, NTSD
8	P, V, Fr, NTSD, preDH		

commonly used model (Bishop, 2006).

$$y(x, w) = w_0 + w_1 x_1 + \ldots + w_D x_D \quad (1)$$

where $x = [x_1, x_2 \ldots x_D]$ is the input feature vector, $w = [w_0, w_1 \ldots w_D]$ is the linear function parameter, and y is the output. An ANN model is a prediction model that can approximate linear and nonlinear relationships. A typical ANN consists of an input layer, an output layer, and one or more hidden layers, with each layer composed of multiple hidden neurons (Haykin, 2009). Random forest, AdaBoost, XGboost and lightGBM are tree algorithms that have been proven to perform well on regression problems based on decision trees (Mienye et al., 2019), and these four algorithms were chosen due to their popular adoption and excellent performance (Pathak et al., 2018).

Fig. 4 shows the model selection process. The dataset from the multi-layer straight-line deposition was divided into training and test data. In the model training process, selection of the hyperparameters of each model is essential and has been reported to influence the model performance dramatically (Zhang et al., 2019). Therefore, validation data are often divided from the training data to perform hyperparameter optimization. Here, the hyperparameters are parameters that control the learning process, and they can be real-valued (e.g., learning rate), integer-valued (e.g., number of layers), binary (e.g., early stopping or not), or categorical (e.g., choice of optimizer) (Hutter et al., 2019). A Bayesian optimization algorithm with k-fold cross-validation was used to determine the best hyperparameters for each model. Once the training was complete, the test set was used to evaluate the performance of each prediction model. The layer height estimation model was selected as the one with the smallest root mean square error (RMSE) among the different algorithms and feature combinations. Next, a DaNN model was established based on the ANN model for layer height estimation of both straight-line and corners during multi-layer corner deposition.

2.3. Development of DaNN model for multi-layer corner deposition

Through straight-line deposition, an ANN model was successfully obtained for layer height estimation. However, the DED process involves both straight-line and corner depositions, and severe layer height deviation often occurs during corner deposition. In this study, the knowledge transfer concept was adopted for layer height estimation during corner deposition, which has been proven to be a more efficiently way for model establishment under such situation (Zhang et al., 2021; Fan et al., 2018). Rather than collecting large amounts of data during corner deposition, utilizing multi-layer straight-line data is preferred when estimating the layer height of corners to save time and effort. In this way, it is essential to consider differences in the formation of straight-line and corner layers, which include one easily observable difference (i.e., traverse speed) and other unobserved differences such as heat accumulation. Therefore, a DaNN model was developed based on previous ANN model using multi-layer straight-line data and corner features including speed revision.

2.3.1. Speed revision

Because the traverse speed often decreases at corners and differs from the as-designed value, the actual traverse speed is measured in real-time by a vision camera and used to replace the as-designed traverse speed in corner features.

The real-time measurement of traverse speed is illustrated in Fig. 5. A vision camera was installed about 1 m away from an artificial marker and the marker was attached to the nozzle to trace the nozzle movement. A camera continuously captured the images, including the marker, during the deposition at a high sampling rate. A template matching algorithm based on normalized cross-correlation (Xu et al., 2018) was then adopted to detect the marker movement in the images. A conversion scale between the pixel unit and the physical length unit was determined using the physical size of the target and its corresponding size in pixel units (Lee and Shinozuka, 2006), so that the movement of marker can be converted from pixel units to physical length units. The actual traverse speed of the nozzle was approximated using the movement of the marker in physical length units.

2.3.2. Model establishment

To utilize multi-layer straight-line data for layer height estimation during multi-layer corner deposition, the domain adaption problem in knowledge transfer is a key issue in this study. The domain adaption is in giving a labeled source domain $D_s = \{x_i, y_i\}$, and an unlabeled target domain $D_t = \{x_j\}$, where x_i and x_j are the feature vectors and y_i is the label. The feature space and label space in the source and target domains are the same, but the data distributions are different, and the goal is to utilize the knowledge from D_s to obtain the label of D_t Ben-David et al. (2010). In this study, the source domain is multi-layer straight-line data, and the target domain refers to the features obtained during multi-layer corner deposition, including straight-line feature and corner feature. To solve the domain adaptation problem, Ghifary et al. (2014) proposed a DaNN model for object recognition which consists of only one hidden layer and one output layer. Through calculating the data distribution difference between the source and target domains by maximum mean discrepancy (MMD) and including the difference in loss function, the

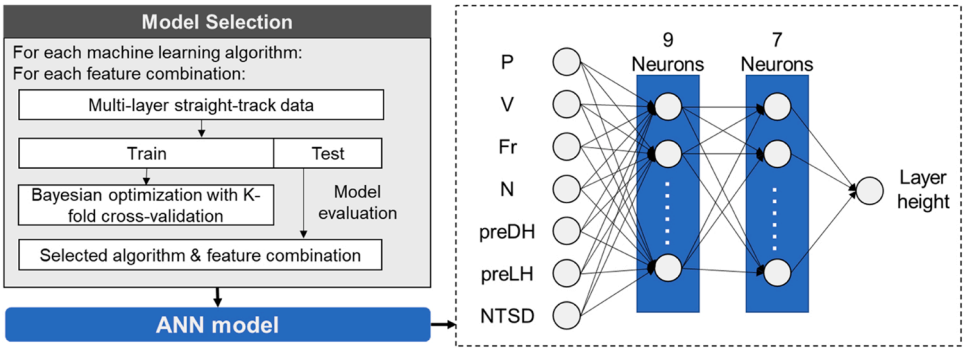

Fig. 4. Model selection process and the selected ANN model.

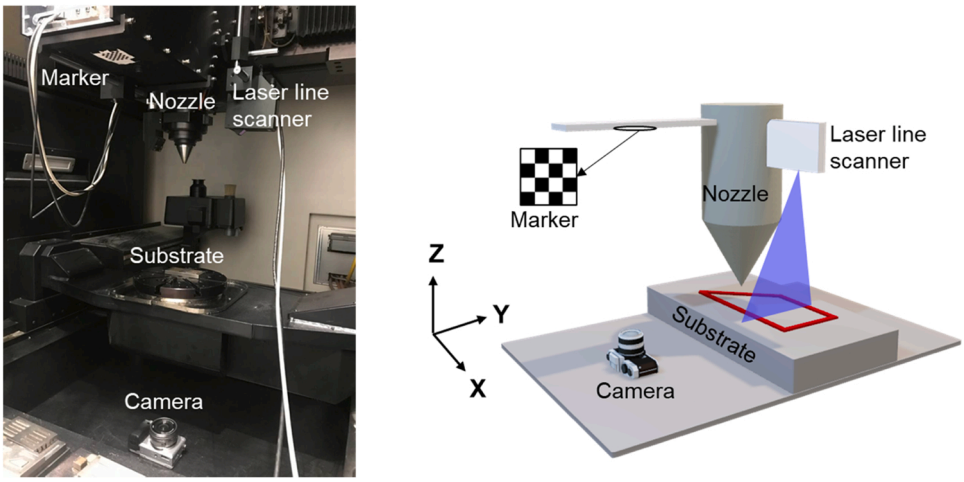

Fig. 5. Traverse speed measurement using vision camera.

network becomes more invariant across different domains.

After obtaining the actual traverse speed, the proposed DaNN model could be established, as shown in Fig. 6. The structure of DaNN model was then revised to include two hidden layers since the best ANN model from previous section was utilized, and the loss function of the neural network of DaNN model was revised to use the MSE loss rather than the empirical log-likelihood loss so that the model can be used for regression rather than classification. As shown in the upper part of Fig. 6, a feed forward neural network was constructed using the ANN model obtained in Section 2.2, described by Eqs. (2) and (3).

$$A^{\langle t\rangle} = W^{\langle t\rangle} X^{\langle t-1\rangle} + B^{\langle t\rangle} \tag{2}$$

$$X^{\langle t\rangle} = g^{\langle t\rangle}\left(A^{\langle t\rangle}\right) \tag{3}$$

where the superscript t represent the particular layer of the network, e.g., $t = 0$ represents the input layer and $t = 1$ represents the first hidden layer. The term $g^{\langle t\rangle}(\bullet)$ represents nonlinear activation function. $A^{\langle t\rangle}$ is a matrix of the linear transformation of the input $X^{\langle t-1\rangle}$, calculated using the weight matrix $W^{\langle t\rangle}$ and bias matrix $B^{\langle t\rangle}$. For example, in the first hidden layer, $A^{\langle 1\rangle}$ consists of $a_j^{\langle 1\rangle}$ where $j = 1, \ldots, M$ and each component $a_j^{\langle 1\rangle}$ is a linear transformation of the input variables $x_1^{\langle 0\rangle}, \ldots x_D^{\langle 0\rangle}$ in the form shown in Eq. (4). The parameters $w_{ji}^{\langle 1\rangle}$ and $b_j^{\langle 1\rangle}$ are referred to as the weights and biases, respectively.

$$a_j^{\langle 1\rangle} = \sum_{i=1}^{D} w_{ji}^{\langle 1\rangle} x_i^{\langle 0\rangle} + b_j^{\langle 1\rangle} \tag{4}$$

The neural network loss (J_{NN}) was calculated using the Mean Squared Error (MSE) loss given source domain label. Then, the target domain input, which contains the features obtained during corner deposition, passed through the same feed forward neural network. An adaptation layer was then added and the MMD loss (J_{MMD}) was calculated using Eq. (5), where γ is a regularization constant determining the importance of the MMD contribution to the loss function. The MMD was calculated by choosing the Gaussian kernel as it has been well studied and proven to be effective for MMD calculation in practice (Gretton et al., 2012). The MMD loss was treated as additional loss and added to the neural network

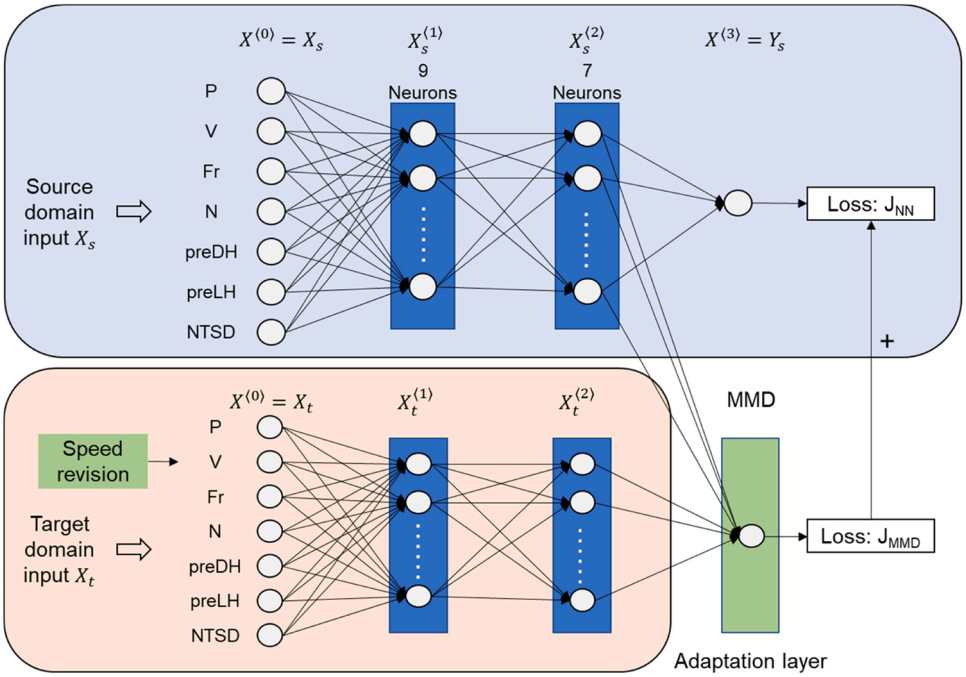

Fig. 6. The established DaNN model.

loss, which forms the final loss function for model training as represented in Eq. (6).

$$J_{MMD} = \gamma MMD^2\left(X_s^{(2)}, X_t^{(2)}\right) \tag{5}$$

$$J_{DaNN} = J_{NN} + J_{MMD} \tag{6}$$

2.4. Online DaNN model updating for accuracy improvement

To further improve the layer height estimation performance, the in-situ data obtained during corner deposition was used as the target domain input for updating the proposed DaNN model, as illustrated in Fig. 1. With multi-layer straight-line data and data batch from corner deposition, speed revision was performed for the corner feature and the DaNN model was trained and used for layer height estimation. Then, this procedure was repeated when more and more data batches were obtained, so that the DaNN model was updated online and expected to remain adaptive for new data, thus achieving better estimation performance.

The real-time layer height estimation can be achieved during deposition by acquiring required features in advance. The features except the traverse speed can be obtained before deposition of the current layer, and the traverse speed can be measured by vision camera with specific frame rate during deposition of current layer. Real-time can be achieved because the layer height can be estimated less than a second during deposition of the current layer.

3. Experiment setup

3.1. Description of directed energy deposition system

A commercial metal DED printer (MX-400 DED from Insstek Inc.) was used in this study and was equipped with ytterbium fiber laser, metal powder carrier, shield gas and carrier gas (Argon gas), and mechanical moving stage. As shown in Fig. 7, metal powders are delivered by carrier gas, melted by the laser beam, and deposited on top of a substrate or previously deposited layer. The mechanical stage with 5 degrees-of-freedom moves the nozzle carrying the laser beam and powder delivery system so that layers can be deposited in different locations and in various shapes. The specifications of DED machine and setup of the printing parameters used in the experiment based on recommendations from the manufacturer of the printer and preliminary experiments are summarized in Table 2. A 1070 nm continuous wave ytterbium fiber laser was used in the Insstek MX-400 DED printer. The recommended optimal laser beam size, carrier gas flow rate, and shield gas flow rate were 800 μm, 2.5 L/min and 5.0 L/min, respectively. In order to ensure the quality of the printed components, the value of laser power, traverse speed and powder feed rate were limited to a range of 300–900 W, 5–15 mm/s, and 3–4 g/min, respectively, based on preliminary experiments. Note that the NTSD should be maintained at 9 mm to achieve the optimal laser beam diameter of 800 μm on the target surface.

Table 2
Specifications of DED machine and printing parameter setup.

DED machine	Insstek MX-400 DED
Laser type	1070 nm Ytterbium fiber laser
Laser beam size	800 μm
Carrier gas flow rate	2.5 L/min
Shield gas flow rate	5.0 L/min
Laser power	300–900 W
Traverse speed	5–15 mm/s
Powder feed rate	3.2–4 g/min

3.2. Design of experiments and description of test specimens

To establish initial layer height estimation model and analyze effects of printing parameters on layer height, data samples from multi-layer straight-line deposition under varying printing parameter conditions were collected. For the design of experiments, a full factorial design (Fisher, 1949) is used in this study as shown in Table 3. The four variable factors were laser power, traverse speed, feed rate and layer number with varying conditions choosing from their recommended range. The recommended ranges for layer power, traverse speed and powder feed rate were listed in Table 2, and the range of layer number was determined as 1–10 by referring to previous literature (Liu et al., 2020). Four conditions of laser power (300, 500, 700, and 900 W), three conditions of traverse speed (5, 10, and 15 mm/s), 3 conditions of feed rate (3.2, 3.6, and 4 g/min), and ten conditions of layer number (1–10 layers) were selected by evenly taking values in each corresponding range. In such case, 360 (= 4 × 3 × 3 × 10) straight-line samples can be collected.

To establish DaNN model for layer height estimation of corner deposition, a small amount of data from multi-layer corner deposition is needed. Therefore, an L-shape specimen was fabricated under a printing parameter condition shown in Table 4, the corner angle had a 90° corner, and the numbers of deposited layers were 1–18. Finally, to validate the proposed layer height estimation method by online

Table 3
Fabrication of multi-layer straight-line under varying printing parameter conditions.

P (W)	V (mm/s)	Fr (g/min)	N
300	5	3.2	1–10
500	10	3.6	
700	15	4	
900			
4 conditions	3 conditions	3 conditions	10 conditions

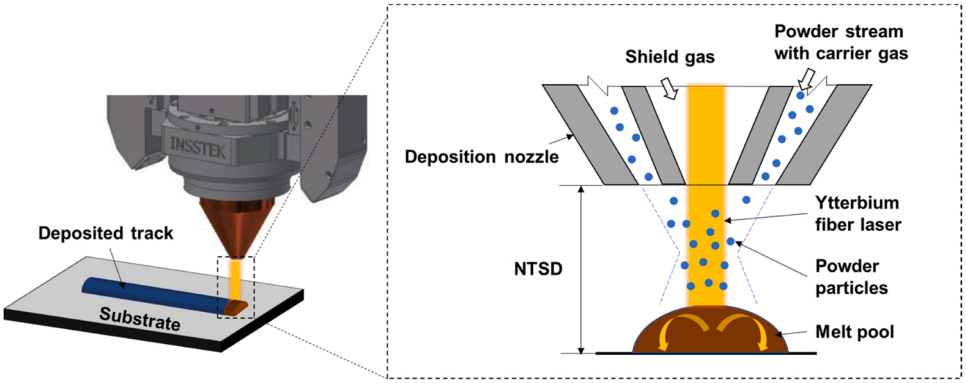

Fig. 7. Description of powder DED system.

Table 4
Fabrication of multi-layer corner deposition under varying printing parameter conditions.

	P (W)	V (mm/s)	Fr (g/min)	N
L-shape	700	10	3.6	1–18
Trapezoid-shape	700	10	3.6	1–18
	600	15	4	1–18
	700	10	3.6	1–18
	500	10	3.2	1–18
	700	15	3.6	1–18

updating DaNN model, multi-layer corner depositions were conducted. The trapezoid-shape specimens were manufactured under five printing parameter conditions as listed in Table 4, with varying corner angles (45°, 90°, and 135°) and layer numbers (1–18 layers).

Test specimens were printed using 316 L stainless steel powder (TLS Technik GmbH & Co. Spezialpul-ver KG). The powder is spherical, with 98% of the powder size between 45 and 150 μm and an average powder size of 100 μm. Powder sizes smaller than 45 μm and larger than 150 μm both account for 1%. Substrates for the deposition of test specimens used 316 L stainless steel with dimensions of 100 mm × 50 mm × 10 mm. As shown in Fig. 8, three types of multi-layer specimens were fabricated under varying printing parameter conditions: (1) straight-line, (2) L-shape, and (3) trapezoid-shape specimens.

4. Experiment results and discussion

4.1. Preliminary data analysis

The layer height was obtained from multi-layer straight-line deposition using laser line scanner as illustrated in Fig. 3. The layer height of the first three layers, referred as LH1, LH2 and LH3, under different deposition conditions were presented in Fig. 9. In general, the layer height increased when the laser power increased, the traverse speed decreased and the feed rate increased, which conformed with existing studies. This was mainly attributed to the change of deposition mass with varying values of the laser power, the traverse speed, and the feed rate. With larger laser power, more energy was provided into the melt pool and more powder was melted, resulting in an increase of deposition mass thus the layer height increased. When the traverse speed decreased, the amount of powder deposited per unit time increased, leading to the increase of layer height. With a larger feed rate, more powder was melted, and the deposition mass increased which led to the layer height increase (Wirth and Wegener, 2018; Liu et al., 2020; Criales et al., 2017).

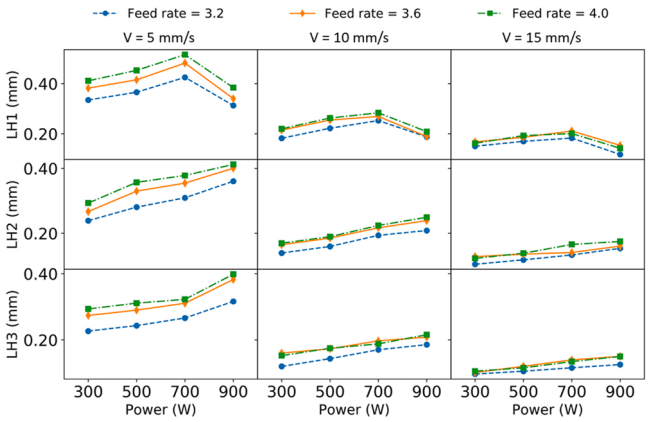

Fig. 9. Layer heights of first three layers under different deposition conditions.

In addition, there were some noteworthy observations. First, for the first layer, the layer height decreased once the laser power exceeded 700 W. The decrease of the layer height might be due to the fact that excessive laser power could drive the liquid metal in the melt pool to flow around under various forces such as gravity and Marangoni convection (Lee and Farson, 2016), causing the melt pool to be more flatten, and resulting in the decrease of the layer height (Liu et al., 2018). Second, at high traverse speeds (15 mm/s), the same change in feed rate had a less significant effect on layer height. Comparison of the second and third columns revealed that the layer heights at the feed rates of 3.6 g/min and 4.0 g/min were almost same and the higher feed rates occasionally resulted in the smaller layer heights. It can be inferred that this is because although the amount of powder increased, only part of

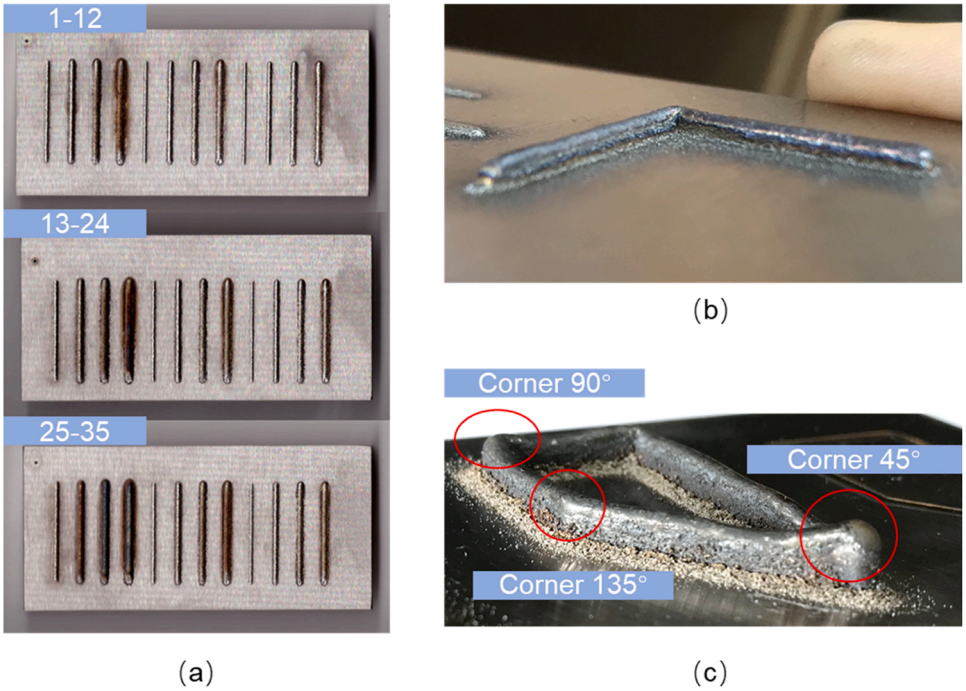

Fig. 8. Test specimens: (a) multi-layer straight-line deposition, (b) multi-layer L-shape deposition and (c) multi-layer trapezoid-shape deposition.

the powder could be melted due to the limited energy provided (Liu and Li, 2007). Overall, it can be observed that the traverse speed had the most significant effect on the layer height.

Fig. 10 shows the comparison of the relationship between the deposition height and the layer number obtained from different corner deposition angles. The deposition height was always the smallest for the straight-line deposition, and the sharper the corner angle, the larger the deposition height. This is most likely due to a more traverse speed reduction occurs at sharp angles (Comminal et al., 2019) and it can be inferred that the slower the traverse speed, the higher the corner height. However, quantitative relationships between traverse speed and deposition height at corners have not been explicitly explained. Besides, the deposition height difference between the corner and straight-line parts increased as more layers were deposited at the corners (45°, 90 °, 135 °) due to cumulative errors, which indicates the necessity of geometry control during corner deposition.

4.2. Results of selection of layer height estimation model

The dataset obtained from the multi-layer straight line deposition was divided into training and test data in a ratio of 0.8 and 0.2, respectively. The training data was used to train each candidate model and the test data was used to evaluate the performance of the candidate models. For each model and each feature combination, a Bayesian optimization algorithm with 5-fold cross validation was used to find the best hyperparameters during the training process. After that, the test data was used to evaluate the performance of each prediction model. Among the candidate prediction models and different feature combinations, the one with the smallest RMSE is selected as the initial model. Fig. 11 shows the RMSEs of the six prediction models with different feature combinations. Among all prediction models, the linear regression model resulted in the worst prediction performance and the ANN model almost always performed the best under different feature combinations. As for feature selection, each prediction model had its own best feature combinations and there was no unique best feature combination across all the prediction models. It was clear that the estimation with only three principal printing parameters (Index 1) was always worse than those considering additional process parameters.

The ANN model with all features (feature combination index 15) achieved the smallest RMSE of 9.8 μm on the test data, and this model consists of two hidden layers with 9 and 7 neurons, respectively, as shown in Fig. 4. Fig. 12 shows the layer estimation performance of the ANN model on the test data.

4.3. Results of development of DaNN model

A SONY α6400 vision camera was used in the experiment with a 34 mm telephoto lens. The camera captured the target images at 60 Hz with a pixel resolution of 1920 × 1080. The conversion scale between the pixel units and the physical length units was calculated to be

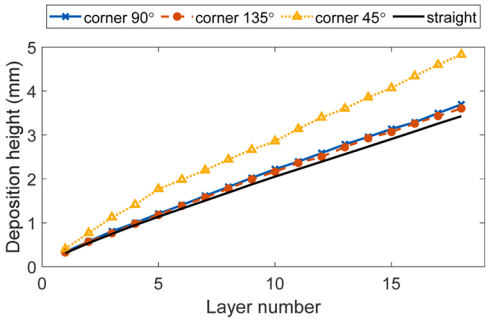

Fig. 10. Comparison of the relationship between the deposition height and layer number at different corner deposition angles.

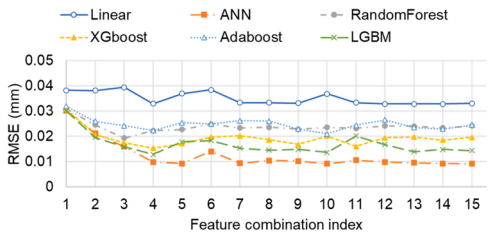

Fig. 11. RMSE of layer height estimation for multi-layer straight-track deposition with different algorithms and feature combinations.

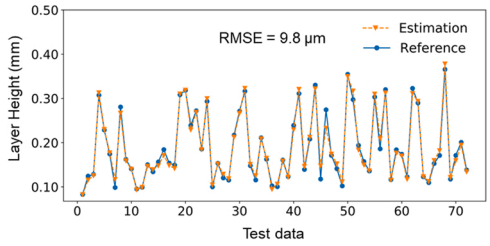

Fig. 12. Layer height estimation for test data using ANN model.

1.166 mm/pixel. The movements of the attached marker in the X and Y axes were tracked and used to calculate the speed along the X and Y axes. The traverse speed was obtained by summing the speed vectors in the X and Y axes. Fig. 13 shows a traverse speed time series recorded during trapezoid-shape specimen deposition. The profile number of each corner can be determined when the speed in X and Y axes change, and the corresponding traverse speed of each corner was obtained, as shown in Fig. 13. The recorded time series reveals that the traverse speed decreased at the corner parts and smaller angles led to larger decreases in the traverse speed at the corners.

After obtaining the traverse speed at the corners, the corner feature was revised accordingly and the DaNN model could be trained based on the multi-layer straight-line data (source domain) and features from the L-shape deposition (target domain). The training process was conducted on GPU (NVIDIA GeForce RTX 2060 SUPER) using Python 3.6, Pytorch 1.10.2 and CUDA 11.3, and the training time took 16 s for 3500 epochs. The constructed ANN model was also applied on the L-shape deposition data for comparison with the DaNN model.

Fig. 14 compares the layer and deposition heights estimated using the DaNN model (orange line) and the ANN model (green line), respectively. The reference layer heights (blue line) were measured by the laser line scanner (Micro-Epsilon scanControl 3000–25/BL). In Fig. 14 (a), the layer height estimation at the 90° corner using the DaNN model provided a much better result (RMSE=14.6 μm) than using the ANN model (RMSE =37.2 μm), validating the effectiveness of the proposed DaNN model. The layer height estimation of the straight-line part using the proposed DaNN model, and the ANN model did not have any significant difference, as the RMSE obtained from DaNN (9.2 μm) and

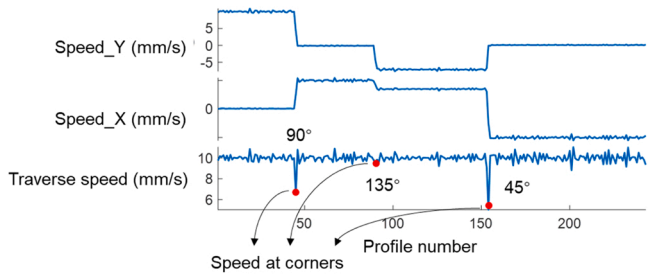

Fig. 13. Example of traverse speed measured during trapezoid-shape deposition.

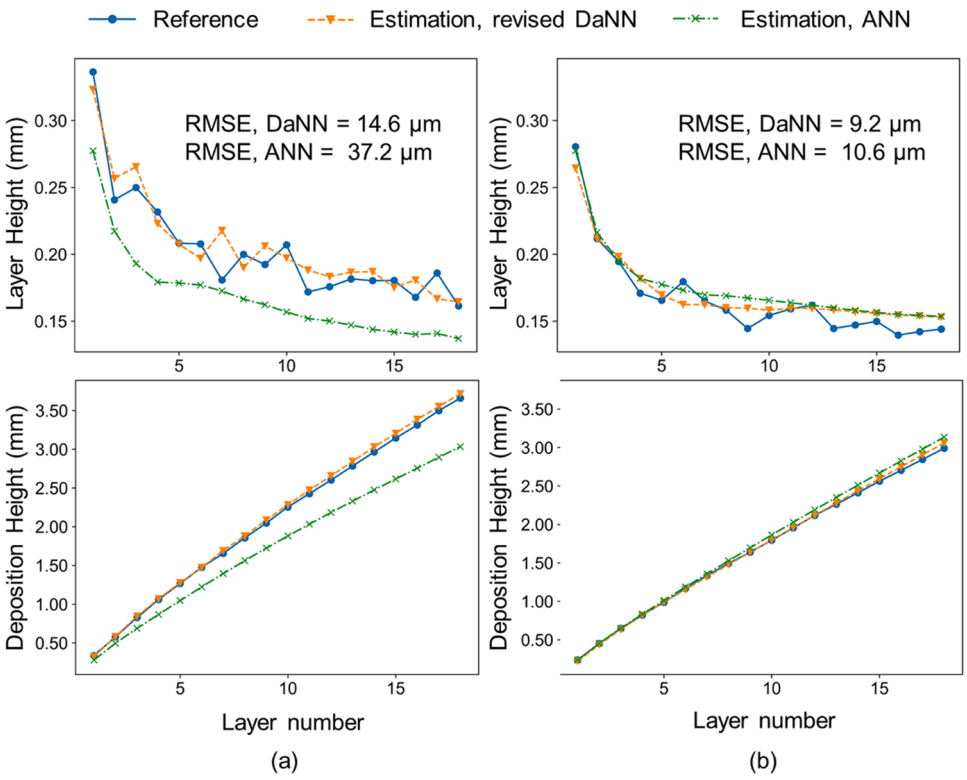

Fig. 14. Comparison of the estimated layer height of (a) 90° corner part and (b) straight-line part, and deposition height of (c) 90° corner part and (d) straight-line part using DaNN model and ANN model during L-shape deposition.

ANN (10.6 μm) are quite similar (Fig. 14 (b)). This result revealed that the proposed DaNN trained after considering corner features could still perform well for straight-line deposition. The DH at each layer was calculated by the accumulation of the layer height of all previous layers, and the result shown in Fig. 14, to gaining a more obvious comparison of the estimation performance. The deposition height in Fig. 14 shows that (1) The deposition height estimated using the DaNN model was close to the reference deposition height; and (2) the error of each layer height estimation did not accumulate as more layers were deposited.

4.4. Results of real-time layer height estimation during multi-layer corner deposition

Once the DaNN model was obtained, real-time layer height estimation was performed during the fabrication of the five specimens shown in Table 3. To further improve the estimation performance during corner deposition, the DaNN model was updated using in-situ data obtained from the trapezoid-shape deposition. Data from each specimen was treated as a data batch to continuously update the DaNN model and the updated DaNN model was used for real-time layer height estimation of the next data batch. The time for updating the DaNN model was about 20 s when new data batches were added, which was considered acceptable since it is common to have several seconds or minutes of preparation time between the deposition of specimens. The layer height estimation using the proposed DaNN model took less than 1 ms for each data sample. The traverse speed is measured at a 60 Hz frame rate, and this is equivalent to a 0.017 s measuring time for each data sample. Therefore, the layer height for the current layer can be estimated within 0.018 s Fig. 15 shows the RMSE of the layer height of each data batch, and a slight improvement can be seen when more data batches were deposited (Table 5).

Fig. 16 shows the real-time layer height estimation results of data batch 5, including 90°, 135°, 45° corner parts and the straight-line part during trapezoid-shape deposition. Similarly, the reference layer height

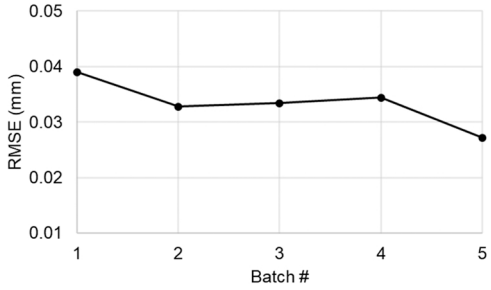

Fig. 15. RMSE of real-time layer height estimation of data batch 1–5.

(blue line) was measured by the laser line scanner. The orange and green lines denote the estimation using the updated DaNN model and the ANN model, respectively. The updated DaNN model achieved better layer height estimation performance than the ANN model for all corners, especially for sharp corner (45°), where the estimated deposition height using the updated DaNN model was much closer to the reference deposition height compared with that using the ANN model.

The improvement achieved by the online updated DaNN model compared with ANN model was calculated using the following equation.

$$\text{Improvement} = \frac{\text{RMSE}_{(\text{DaNN})} - \text{RMSE}_{(\text{ANN})}}{\text{Average layer height}} \tag{7}$$

where $\text{RMSE}_{(\text{DaNN})}$ and $\text{RMSE}_{(\text{ANN})}$ are the RMSE value of the layer height estimation obtained using the updated DaNN model and ANN model, respectively. Table 4 and Fig. 17 show the layer height estimation results using the ANN model and the improvement achieved by updated DaNN model. The updated DaNN substantially improved the layer height estimation during corner deposition, and the improvement was more significant particularly for smaller corner angles because the traverse speed decrease more significantly at corners with smaller

Table 5
layer height estimation using the updated DaNN model and the ANN model.

Trapezoid-shape	RMSE (μm)	Improvement		
Corner	Batch #	Updated DaNN	ANN	
Corner 135°	1	33.6	43.6	5.3%
	2	19.7	37.1	8.9%
	3	20.9	34.0	6.1%
	4	22.7	36.8	7.4%
	5	27.6	39.7	6.1%
Corner 90°	1	30.3	47.4	9.0%
	2	18.6	42.0	12.0%
	3	25.0	42.6	8.2%
	4	17.6	38.9	11.2%
	5	17.2	49.1	16.0%
Corner 45°	1	54.1	128.3	39.1%
	2	37.1	124.2	44.7%
	3	39.7	115.9	35.4%
	4	28.4	103.8	39.5%
	5	30.2	130.8	50.3%
Straight	1	14.5	16.7	1.2%
	2	16.7	19.6	1.5%
	3	19.6	22.6	1.4%
	4	21.6	25.9	2.3%
	5	19.6	23.9	2.2%
Average RMSE	25.7			

angles. The overall RMSE of real-time layer height estimation during corner deposition with different angles was calculated as 25.7 μm when the typical layer height was about 250 μm.

5. Conclusions

In this study, a real-time layer height estimation technique is developed for DED based multi-layer corner deposition. Layer height estimation model is constructed by considering not only three principal printing parameters (P, V, Fr) but also additional process parameters (N, preLH, preDH, NTSD), and it could achieve better performance than considering only the three principal process parameters. Layer height estimation of the corner part and straight-line part during corner deposition is achieved by utilizing straight-line data and a DaNN model, which saves the time and effort in collecting a large amount of data during corner deposition for training. Finally, real-time layer height estimation was achieved during corner deposition with the online updated DaNN model, with the best estimation performance and layer height estimation for corners with different angles validated.

Although the proposed method has been validated at three different angles (45°, 90° and 135°), a more comprehensive analysis for additional angles should be achieved in future study. Also, the layer width of the corner part is not investigated here, because the layer width did not change much at the corner points based on our preliminary experiments. If necessary, a similar framework can be used for layer width estimation. The experimental results in this study reveal that traverse speed, powder feed rate and laser power can be used to achieve geometry control, and additional process parameters also influence layer height. Therefore, a follow-up study is warranted for layer height control by changing the toolpath, powder feed rate and laser power with consideration of

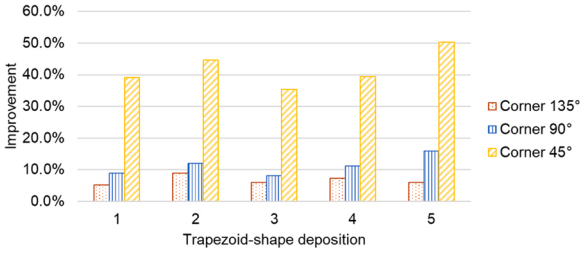

Fig. 17. Improvement of layer height estimation achieved by proposed method.

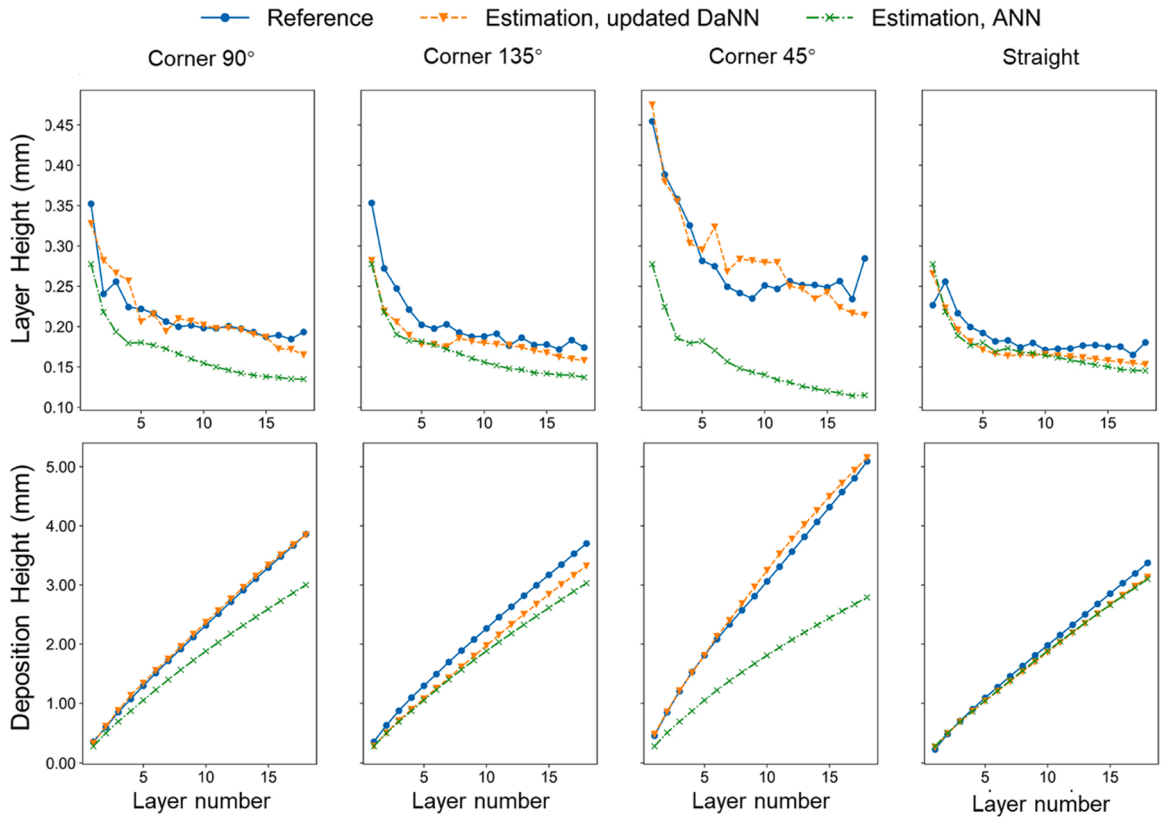

Fig. 16. Real-time layer height estimation during corner deposition, data batch 5.

additional process parameters during corner deposition, especially for sharp corners.

Declaration of Competing Interest

The authors declare that they have no known competing financial interests or personal relationships that could have appeared to influence the work reported in this paper.

Data availability

Data will be made available on request.

Acknowledgement

This work was supported by a National Research Foundation of Korea (NRF) grant funded by the Korean government (MSIT) (grant number: 2019R1A3B3067987).

References

Alya, S., Singh, R., 2021. Discrete phase modeling of the powder flow dynamics and the catchment efficiency in laser directed energy deposition with inclined coaxial nozzles. J. Manuf. Sci. Eng. 143, 081004 https://doi.org/10.1115/1.4049966.

ASTM Committee, Standard terminology for additive manufacturing technologies, ASTM International, 2012.

Bayat, M., Nadimpalli, V.K., Biondani, F.G., Jafarzadeh, S., Thorborg, J., Tiedje, N.S., Bissacco, G., Pedersen, D.B., Hattel, J.H., 2021. On the role of the powder stream on the heat and fluid flow conditions during Directed Energy Deposition of maraging steel—Multiphysics modeling and experimental validation. Addit. Manuf. 43, 102021 https://doi.org/10.1016/j.addma.2021.102021.

Ben-David, S., Blitzer, J., Crammer, K., Kulesza, A., Pereira, F., Vaughan, J.W., 2010. A theory of learning from different domains. Mach. Learn 79, 151–175. https://doi.org/10.1007/s10994-009-5152-4.

Binega, E., Yang, L., Sohn, H., Cheng, J.C.P., 2022. Online geometry monitoring during directed energy deposition additive manufacturing using laser line scanning. Precis. Eng. 73, 104–114. https://doi.org/10.1016/j.precisioneng.2021.09.005.

Bishop, C.M., 2006. Pattern Recognition and Machine Learning. Springer, New York.

Caiazzo, B., Di Nardo, M., Murino, T., Petrillo, A., Piccirillo, G., Santini, S., 2022. Towards Zero Defect Manufacturing paradigm: A review of the state-of-the-art methods and open challenges. Comput. Ind. 134, 103548 https://doi.org/10.1016/j.compind.2021.103548.

Chabot, A., Rauch, M., Hascoët, J.-Y., 2019. Towards a multi-sensor monitoring methodology for AM metallic processes. Weld. World 63, 759–769. https://doi.org/10.1007/s40194-019-00705-4.

Comminal, R., Serdeczny, M.P., Pedersen, D.B., Spangenberg, J., 2019. Motion planning and numerical simulation of material deposition at corners in extrusion additive manufacturing. Addit. Manuf. 29, 100753 https://doi.org/10.1016/j.addma.2019.06.005.

Criales, L.E., Arısoy, Y.M., Lane, B., Moylan, S., Donmez, A., Özel, T., 2017. Predictive modeling and optimization of multi-track processing for laser powder bed fusion of nickel alloy 625. Addit. Manuf. 13, 14–36. https://doi.org/10.1016/j.addma.2016.11.004.

Davim, J.P., Oliveira, C., Cardoso, A., 2008. Predicting the geometric form of clad in laser cladding by powder using multiple regression analysis (MRA. Mater. Des. 29, 554–557. https://doi.org/10.1016/j.matdes.2007.01.023.

Ertay, D.S., Vlasea, M., Erkorkmaz, K., 2020. Thermomechanical and geometry model for directed energy deposition with 2D/3D toolpaths. Addit. Manuf. 35, 101294 https://doi.org/10.1016/j.addma.2020.101294.

Fan, Y., Liu, C., Wang, J., 2018. Integrating multi-granularity model and similarity measurement for transforming process data into different granularity knowledge. Adv. Eng. Inform. 37, 88–102. https://doi.org/10.1016/j.aei.2018.04.012.

Fisher, R.A. (Ed.), 1949. The Design of Experiments, 5th.,. Oliver & Boyd, Oxford, England.

M. Ghifary, W.B. Kleijn, M. Zhang, Domain Adaptive Neural Networks for Object Recognition, ArXiv:1409.6041 [Cs, Stat], 2014. http://arxiv.org/abs/1409.6041 (accessed April 12, 2022).

Gretton, A., Borgwardt, K.M., Rasch, M.J., Schölkopf, B., Smola, A., 2012. A kernel two-sample test. J. Mach. Learn. Res. 13, 723–773.

Haykin, S.S., 2009. Neural Networks and Learning Machines, 3rd ed. Prentice Hall, New York,.

Hutter, F., Kotthoff, L., Vanschoren, J. (Eds.), 2019. Automated Machine Learning: Methods, Systems, Challenges. Springer International Publishing, Cham. https://doi.org/10.1007/978-3-030-05318-5.

Kono, D., Maruhashi, A., Yamaji, I., Oda, Y., Mori, M., 2018. Effects of cladding path on workpiece geometry and impact toughness in Directed Energy Deposition of 316L stainless steel. CIRP Ann. 67, 233–236. https://doi.org/10.1016/j.cirp.2018.04.087.

Lee, J.J., Shinozuka, M., 2006. A vision-based system for remote sensing of bridge displacement. NDT E Int. 39, 425–431. https://doi.org/10.1016/j.ndteint.2005.12.003.

Lee, Y.S., Farson, D.F., 2016. Surface tension-powered build dimension control in laser additive manufacturing process. Int J. Adv. Manuf. Technol. 85, 1035–1044. https://doi.org/10.1007/s00170-015-7974-5.

Li, R., Jin, M., Paquit, V.C., 2021. Geometrical defect detection for additive manufacturing with machine learning models. Mater. Des. 206, 109726 https://doi.org/10.1016/j.matdes.2021.109726.

Liu, F.Q., Wei, L., Shi, S.Q., Wei, H.L., 2020. On the varieties of build features during multi-layer laser directed energy deposition. Addit. Manuf. 36, 101491 https://doi.org/10.1016/j.addma.2020.101491.

Liu, H., Qin, X., Huang, S., Hu, Z., Ni, M., 2018. Geometry modeling of single track cladding deposited by high power diode laser with rectangular beam spot. Opt. Lasers Eng. 100, 38–46. https://doi.org/10.1016/j.optlaseng.2017.07.008.

Liu, J., Li, L., 2007. Effects of process variables on laser direct formation of thin wall. Opt. Laser Technol. 39, 231–236. https://doi.org/10.1016/j.optlastec.2005.08.012.

Liu, P., Yi, K., Jeon, I., Sohn, H., 2021. Porosity inspection in directed energy deposition additive manufacturing based on transient thermoreflectance measurement. NDT E Int. 122, 102491 https://doi.org/10.1016/j.ndteint.2021.102491.

Mienye, I.D., Sun, Y., Wang, Z., 2019. Prediction performance of improved decision tree-based algorithms: a review. Procedia Manuf. 35, 698–703. https://doi.org/10.1016/j.promfg.2019.06.011.

S. Pathak, I. Mishra, A. Swetapadma, An Assessment of Decision Tree based Classification and Regression Algorithms, in: 2018 3rd International Conference on Inventive Computation Technologies (ICICT), IEEE, Coimbatore, India, 2018: pp. 92–95. https://doi.org/10.1109/ICICT43934.2018.9034296.

Pereira, J.C., Borovkov, H., Zubiri, F., Guerra, M.C., Caminos, J., 2021. Optimization of Thin Walls with Sharp Corners in SS316L and IN718 Alloys Manufactured with Laser Metal Deposition. JMMP 5, 5. https://doi.org/10.3390/jmmp5010005.

Pinkerton, A.J., Li, L., 2004. Modelling the geometry of a moving laser melt pool and deposition track via energy and mass balances. J. Phys. D: Appl. Phys. 37, 1885–1895. https://doi.org/10.1088/0022-3727/37/14/003.

Snoek, J., Larochelle, H., Adams, R.P., 2012. Practical Bayesian Optimization of Machine Learning Algorithms. In: Advances in Neural Information Processing Systems. Curran Associates, Inc. https://proceedings.neurips.cc/paper/2012/hash/05311655a15b75fab86956663e1819cd-Abstract.html (accessed December 8, 2022).

Sun, Z., Guo, W., Li, L., 2020. Numerical modelling of heat transfer, mass transport and microstructure formation in a high deposition rate laser directed energy deposition process. Addit. Manuf. 33, 101175 https://doi.org/10.1016/j.addma.2020.101175.

Thakkar, D., Sahasrabudhe, H., 2020. Investigating microstructure and defects evolution in laser deposited single-walled Ti6Al4V structures with sharp and non-sharp features. J. Manuf. Process. 56, 928–940. https://doi.org/10.1016/j.jmapro.2020.05.052.

Tyralla, D., Köhler, H., Seefeld, T., Thomy, C., Narita, R., 2020. A multi-parameter control of track geometry and melt pool size for laser metal deposition. Procedia CIRP 94, 430–435. https://doi.org/10.1016/j.procir.2020.09.159.

Vandone, A., Baraldo, S., Valente, A., 2018. Multisensor data fusion for additive manufacturing process control. IEEE Robot. Autom. Lett. 3, 3279–3284. https://doi.org/10.1109/LRA.2018.2851792.

Walker, T.R., Bennett, C.J., Lee, T.L., Clare, A.T., 2020. A novel numerical method to predict the transient track geometry and thermomechanical effects through in-situ modification of the process parameters in Direct Energy Deposition. Finite Elem. Anal. Des. 169, 103347 https://doi.org/10.1016/j.finel.2019.103347.

Q. Wang, J. Li, M. Gouge, A.R. Nassar, P. Michaleris, E.W. Reutzel, Reduced-order multivariable modeling and nonlinear control of melt-pool geometry and temperature in directed energy deposition, in: 2016 American Control Conference (ACC), IEEE, Boston, MA, USA, 2016: pp. 845–851. https://doi.org/10.1109/ACC.2016.7525019.

Wang, R., Cheung, C.F., Wang, C., Cheng, M.N., 2022. Deep learning characterization of surface defects in the selective laser melting process. Comput. Ind. 140, 103662 https://doi.org/10.1016/j.compind.2022.103662.

Wang, S., Zhu, L., Fuh, J.Y.H., Zhang, H., Yan, W., 2020. Multi-physics modeling and Gaussian process regression analysis of cladding track geometry for direct energy deposition. Opt. Lasers Eng. 127, 105950 https://doi.org/10.1016/j.optlaseng.2019.105950.

Wirth, F., Wegener, K., 2018. A physical modeling and predictive simulation of the laser cladding process. Addit. Manuf. 22, 307–319. https://doi.org/10.1016/j.addma.2018.05.017.

Woo, Y.-Y., Han, S.-W., Oh, I.-Y., Moon, Y.-H., Ha, W., 2019. Control of directed energy deposition process to obtain equal-height rectangular corner. Int. J. Precis. Eng. Manuf. 20, 2129–2139. https://doi.org/10.1007/s12541-019-00226-6.

Xiong, J., Zhang, G., 2014. Adaptive control of deposited height in GMAW-based layer additive manufacturing. J. Mater. Process. Technol. 214, 962–968. https://doi.org/10.1016/j.jmatprotec.2013.11.014.

Xu, Y., Brownjohn, J., Kong, D., 2018. A non-contact vision-based system for multipoint displacement monitoring in a cable-stayed footbridge. Struct. Control Health Monit. 25, e2155 https://doi.org/10.1002/stc.2155.

Zhang, H., Choi, J.P., Moon, S.K., Ngo, T.H., 2021. A knowledge transfer framework to support rapid process modeling in aerosol jet printing. Adv. Eng. Inform. 48, 101264 https://doi.org/10.1016/j.aei.2021.101264.

Zhang, X., Chen, X., Yao, L., Ge, C., Dong, M., 2019. Deep neural network hyperparameter optimization with orthogonal array tuning. In: Gedeon, T., Wong, K. W., Lee, M. (Eds.), Neural Information Processing. Springer International Publishing, Cham, pp. 287–295. https://doi.org/10.1007/978-3-030-36808-1_31.